Time-lapse 3D inversion of complex conductivity data using an active time constrained (ATC) approach

M. Karaoulis (1), A. Revil (1,2), A., D.D. Werkema (3), B. Minsley (4),

W.F. Woodruff (1), and A. Kemna (5)

(1) Colorado School of Mines, Dept. of Geophysics, Golden, CO, USA.
(2) ISTerre, CNRS, UMR 5559, Université de Savoie, Equipe Volcan, Le Bourget du Lac, France.
(3) U.S. EPA, ORD, NERL, ESD, CMB, Las Vegas, Nevada, USA .
(4) USGS, Federal Center, Lakewood, 10, 80225-0046, CO.
(5) Dept. of Geodynamics and Geophysics, University of Bonn, Nussallee 8, 53115, Bonn, Germany.

Short Title: Time-lapse complex conductivity imaging

Corresponding author: André Revil (arevil@mines.edu)

Email from the co-authors: arevil@mines.edu; bminsley@usgs.gov; kemna@geo.uni-bonn.de; Werkema.D@epamail.epa.gov, wfwoodruff@gmail.com, mkaraoulis@mines.edu

GJI Section: Marine geosciences and applied geophysics

Key-words: Electrical properties; Hydrogeophysics; Permeability and porosity.

Intended for publication in Geophysical Journal International

Summary. Induced polarization (more precisely the magnitude and the phase of the impedance of the subsurface) is measured using a network of electrodes located at the ground surface or in boreholes. This method yields important information related to the distribution of permeability and contaminants in the shallow subsurface. We propose a new time-lapse 3D modeling and inversion algorithm to image the evolution of complex conductivity over time. We discretize the subsurface using hexahedronal cells. Each cell is assigned a complex resistivity or conductivity value. Using the finite-element approach, we model the in-phase and out-of-phase (quadrature) electrical potentials on the 3D grid, which are then transformed into apparent complex resistivity. Inhomogeneous Dirichlet boundary conditions are used at the boundary of the domain. The calculation of the Jacobian matrix is based on the principles of reciprocity. The goal of time-lapse inversion is to determine the change in the complex resistivity of each cell of the spatial grid as a function of time. Each model along the time axis is called a "reference space model". This approach can be simplified into an inverse problem looking for the optimum of several reference space models using the approximation that the material properties vary linearly in time between two subsequent reference models. Regularizations in both space domain and time domain reduce inversion artifacts and improve the stability of the inversion problem. In addition, the use of the time-lapse equations allows the simultaneous inversion of data obtained at different times in just one inversion step (4D inversion). The advantages of this new inversion algorithm are demonstrated on synthetic time-lapse data resulting from the simulation of a salt tracer test in an heterogeneous random material described by an anisotropic semi-variogram.

1. Introduction

Electrical resistivity is sensitive to salinity, porosity, saturation, pore shape, temperature, clay content, and biological activity (e.g., Waxman & Smits, 1968; Revil *et al.*, 1998; Atekwana *et al.*, 2004). Variability in any of these parameters can have an influence on resistivity and can be monitored by time-lapse electrical resistivity tomography (TL-ERT). In the recent literature, TL-ERT has started to be a popular method to monitor dynamic processes occurring in the shallow subsurface (typically the first hundred meters, see Legaz *et al.*, 2009, Müller *et al.*, 2010 and references therein). TL-ERT imaging, often involving permanent electrode installations, has proven to provide information complementary to in situ geochemical measurements. Applications of TL-ERT include monitoring of subsurface flow (e.g., Daily *et al.*, 1992; Ramirez *et al.*, 1993; Park, 1998; Daily & Ramirez, 2000; Nimmer *et al.*, 2007), characterization of solute transport (e.g., Slater *et al.*, 2000; Kemna *et al.*, 2002; Singha & Gorelick, 2005; Looms *et al.*, 2008), saturation and temperature (Legaz *et al.*, 2009), and mapping of salt-water intrusion in aquifers (e.g., Nguyen *et al.*, 2009; Ogilvy *et al.*, 2009) just to cite few applications.

In an effort to extract more information about the subsurface geology (e.g., shale versus brine-saturated sands), the distribution of permeability, and the distribution of contaminants or to observe change in the precipitation of metallic particles (resulting from changes in the redox conditions) during bioremediation, resistivity measurements can be extended in the frequency domain, typically in the range from 1 mHz to 1 kHz in the laboratory and 10 mHz to 100 Hz in the field (e.g., Olhoeft, 1985, 1986; Borner *et al.*, 1996; Lesmes & Morgan, 2001; Kemna *et al.*, 2004; Vanhala, 2007; Nordsiek & Weller, 2008; Williams *et al.*, 2009; Flores-Orozco *et al.*, in press). Such a geophysical method is called complex resistivity, complex conductivity, (time-domain or frequency-domain) induced polarization, or low-frequency dielectric spectroscopy in the literature. In frequency-domain induced polarization, an alternating current is injected and retrieved into the ground using two electrodes A and B. Both the resulting magnitude and the phase of the voltage between two potential electrodes M and N are measured and used to define an impedance, which once corrected for the position of the electrode is used to define an apparent complex resistivity. This method was originally developed for the exploration of ore bodies (see Pelton *et al*., 1978, Seigel *et al*., 2007). The sensitivity enhancement of modern equipment has increased the measurement resolution of the phase lag between the current and the voltage (typically 0.1 mrad in the laboratory up to 100 Hz and 0.4 mrad in the field with a 24 bit acquisition card, see discussion in Vaudelet *et al*., 2011a, b and G. Olhoeft, personal communication, 2010). This instrumentation has made possible the use of the induced polarization method in environmental investigations (for which the phase lag is usually very small, <20 mrad) such as the detection of organic and inorganic contaminants (Olhoeft, 1985, 1986; Börner *et al*., 1993; Schmutz *et al*., 2010) and the determination of permeability (e.g., Börner *et al*., 1996; Binley *et al*., 2005; Hördt *et al*., 2007; Kemna *et al*., 2004; Revil & Florsch, 2010).

Recently, Revil and co-workers (Leroy *et al*., 2008; Leroy & Revil, 2009; Schmutz *et al*., 2010; Revil & Florsch, 2010) have also provided a complete theoretical framework explaining induced polarization measurements in terms of polarization of the electrical double layer coating the surface of the grains. They followed previous works done by de Lima & Sharma (1992) and Lesmes & Morgan (2001). However, all these approaches do not include a description of membrane polarization and a unified model including this contribution has still to be done. The approach described in Leroy *et al*. (2008) can be used to provide a physical explanation for the Cole-Cole model, which is broadly used to interpret induced polarization measurements in the laboratory or in the field (see Pelton *et al*., 1978; Ghorbani *et al*., 2007; Florsch *et al*. 2010).

Several single time step inversion algorithms have been proposed to invert induced polarization data, either involving frequency-domain complex resistivity modeling (Kemna & Binley, 1996; Shi *et al*., 1998; Kemna *et al*., 2000) or time-domain chargeability modeling (Routh *et al*., 1998; Loke *et al.,* 2006). The introduction of time into the inversion of geophysical data sets can be achieved with the use of time-lapse algorithms. In this case, several strategies are possible to perform such a time-lapse inversion. A standard approach is to independently invert the measured data acquired at each monitoring step and to reconstruct time-lapse images (e.g. Daily *et al.,* 1992; Ramirez, 1993; Binley, 1996). As suggested by several researchers, the independent time-lapse inversion images may be strongly contaminated with inversion artifacts due to the presence of noise in the measurements and independent inversion errors. LaBrecque & Young (2001) and Kim *et al*. (2009) presented time-lapse algorithms to minimize those artifacts, but as shown by Karaoulis *et al*. (2011), these algorithmes may also suppress real changes in the complex resistivity due to the spurious effect associated with the selection of the time regularization parameter in the cost function.

In the present work, we describe a new induced polarization time-lapse tomography algorithm. Forward modeling is presented in Section 2. In Section 3, we present a new 4D algorithm for induced polarization based on an Active Time Constrained (ATC) approach. Our work extends the recent work of Karaoulis *et al.* (2011) for DC resistivity to complex resistivity in the frequency domain. Time-lapse time-domain IP data could be treated the same way. In our approach, the subsurface is defined as a space-time model, and the regularization over time is active where it allows variability between different time steps depending on the degree of spatial complex resistivity changes occurring among different monitoring stages (time-steps). As a result, the 4D-ATC algorithm can help in focusing on the 3D spatio-temporal changes of the complex resistivity. We will present results for a single-frequency application of the algorithm; however, the extension of the algorithm to multifrequency time-lapse data can be done with the successive application of the algorithm to a set of data taken at distinct frequencies. Along the same lines, the approach of Kemna *et al.* (1999, 2000) for "static" spectral data provides information about the spectral behavior of the subsurface complex resistivity. Using spectral-induced polarization data, a relaxation model such as the Cole-Cole model can be fitted for each cell and the evolution of the Cole-Cole parameters can be followed over time.

2. Forward Modeling

In the frequency domain, we denote $\omega = 2\pi f$ the angular frequency, f the frequency (in Hertz), and $i = (-1)^{1/2}$ the imaginary unit. The magnitude of the conductivity $|\sigma|$ and the phase lag $\varphi \in [-\pi, \pi)$ between the excitation current and the resulting electrical field are related to the real (in-phase) and imaginary (out-of-phase or quadrature) components of the complex conductivity σ^*, σ' and σ'', respectively, (expressed in S m^{-1}), by

$$\sigma^* = |\sigma| \exp(i\varphi) = \sigma' + i\sigma''. \tag{1}$$

In this equation, $|\sigma| = (\sigma'^2 + \sigma''^2)^{1/2}$ and $\varphi = \operatorname{atan} \sigma''/\sigma'$ represents frequency dependent amplitude and phase of conductivity, respectively. Induced polarization is usually displayed as a resistivity (or conductivity) magnitude $|\rho| = 1/|\sigma|$ (in ohm m) and a phase lag φ (in rad) or alternatively as an in-phase conductivity σ' and a quadrature conductivity σ'', respectively. The complex conductivity is related to the complex resistivity ρ^* by,

$$\sigma^* = \frac{1}{\rho^*}, \tag{2}$$

where $\rho^* \neq 0$. In practice, an alternating current is used to perform spectral or frequency-domain IP measurements. For a given current, both the amplitude of the voltage and the phase lag between the current and the voltage are measured. The impedance can be multiplied by the same geometrical factor as used for DC-resistivity (e.g. Kemna, 2000) in order to provide the amplitude of the apparent electrical conductivity at each frequency. The phase lag is however independent of the geometric factor.

In the forward modeling of the induced polarization problem, the electric potential can be expressed expressed as a complex number (e.g., Kemna, 2000):

$$V(\omega) = V'(\omega) + iV''(\omega). \tag{3}$$

The amplitude of the voltage and the phase lag are given by,

$$|V(\omega)| = \sqrt{[V'(\omega)]^2 + [V''(\omega)]^2}, \tag{4}$$

$$\varphi(\omega) = \text{atan}\left[\frac{V''(\omega)}{V'(\omega)}\right]. \tag{5}$$

In the following, we will neglect electromagnetic coupling effects, which is a good approximation at low frequencies (<100 Hz, see e.g. Kemna, 2000).

The relation between the complex conductivity and the complex potential is given by (Weller *et al.*, 1996)

$$\nabla \cdot [\sigma(x,\omega)\nabla V(x,\omega)] = -I(\omega)\delta(\boldsymbol{x} - \boldsymbol{x}_S), \tag{6}$$

where $\boldsymbol{x}$ is the position vector and $I(\omega)$ is the injected current (in Ampere) at frequency ω represented as a point source at position $\boldsymbol{x}_{S,}$ where δ represents a delta function.

Equation (6) is a Poisson equation, which can be solved for given boundary conditions using the finite-element method (Kemna, 2000). The basic concept of the finite-element method is to subdivide the investigated domain into n_e elements in which the unknown potential $V(\omega)$ is approximated by means of discrete values at the nodes of the elements. Assuming homogeneous and isotropic elements, the solution of the Poisson equation can be obtained in discrete form by solving a system of linear equations:

$$\boldsymbol{K}(\omega)\boldsymbol{V} = \boldsymbol{F}, \qquad (7)$$

where the kernel matrix $\boldsymbol{K}(\omega)$ ($n_e \times n_e$) consists of individual element matrices of each element; these are the same as for the real-valued (DC) problem since all terms are related only to the nodal coordinates, and the multiplication with the complex resistivity transforms the system into a relationship involving complex numbers. The explicit form of this matric for the hexahedron elements used below is given in Tsourlos (1999). The vector $\boldsymbol{V}$ contains the nodal values of the complex potential, and the vector $\boldsymbol{F}$ (n elements) contains the current sources.

In this work we use mixed boundary conditions, which can be implemented in the complex case analogous to the DC case (Kemna, 2000). A Neumann boundary condition is imposed at the ground surface (there is no current flow normal to this boundary), and a finite value is set on the half-space boundaries, which is determined via the asymptotic behavior of the potential for a homogeneous half-space (Dey & Morrison, 1979).

3. Time-Lapse Inversion

We present now the 4D algorithm used to perform the time-lapse inversion. Kim *et al*. (2009) defines the subsurface as a space-time model, which encompasses all space models during the entire monitoring period. The entire monitoring data are defined as a data vector in the space-time domain as well. The space-time model is assumed to change continuously along the time-axis, which allows the change of the subsurface material property distribution during the measurement of the geophysical datum. Assuming a model that is sparsely sampled at pre-selected times, the 4D subsurface model $\tilde{\boldsymbol{X}}$ for all the time steps of the monitoring data is expressed as $\tilde{\boldsymbol{X}} = [\boldsymbol{X}_1, \cdots, \boldsymbol{X}_t]^T$ where $\boldsymbol{X}_i$ is the reference space model, a matrix of complex elements describing the complex resistivity distribution, for the i[th] time step and t denotes the number of monitoring times. The data misfit vector is defined in the space-time domain by

$$\boldsymbol{e}^{k+1} = \hat{\boldsymbol{D}} - G(\tilde{\boldsymbol{X}}^{k+1}) = \hat{\boldsymbol{D}} - G(\tilde{\boldsymbol{X}}^{k} + d\tilde{\boldsymbol{X}}), k = 1,2,\ldots. \tag{8}$$

In Eq. (8), $\hat{\boldsymbol{D}}$ denotes the data vector defined in the 4D coordinate system by $\hat{\boldsymbol{D}} = [\boldsymbol{d}_1, \cdots, \boldsymbol{d}_t]^T$, where $\boldsymbol{d}_i$ is the data from time step i expressed as a complex number describing the alternating potential, $G(\tilde{\boldsymbol{X}}^k)$ denotes the forward modeling response, and $d\tilde{\boldsymbol{X}} = [d\boldsymbol{X}_1, \cdots, d\boldsymbol{X}_t]^T$ is the model perturbation vector, i.e. $d\tilde{\boldsymbol{X}} = \tilde{\boldsymbol{X}}^{k+1} - \tilde{\boldsymbol{X}}^k$, and the superscript k denotes the iteration number.

Since both the data and the model are defined using space-time coordinates, the 4D-ATC algorithm is able to adopt two regularizations, in both the time and space domains, to stabilize the inversion. Consequently, we are looking to minimize the following objective function T (Zhang *et al*., 2005; Kim *et al*., 2009),

$$T = \left\|\boldsymbol{e}^T \boldsymbol{e}\right\|^2 + \lambda\Psi + \alpha\,\Xi\,, \tag{9}$$

where Ψ and Ξ are the two regularization functions/ penalty terms. The function Ψ is used for smoothness regularization in space and the function Γ is used for smoothness regularization in time. The two parameters λ and α are the regularization parameters (also called the Lagrange parameters in the literature). Regarding the smoothness in the space domain, a second-order differential operator is applied to the model perturbation vector $d\hat{\boldsymbol{X}}$. In the time domain, Kim *et al*. (2009) applied a first-order differential operator to the model vector $\hat{\boldsymbol{X}}$. This assumption is consistent with the idea that the change over time of the material properties is smaller compared to their changes in space. Therefore, in our approach, the subsurface structure remains nearly the same throughout the entire monitoring period. Following these principles, the two regularization functions in the cost function, Eq. (9), Ψ and Ξ, are defined as

$$\Psi = (\partial^2 d\hat{\boldsymbol{X}})^T (\partial^2 d\hat{\boldsymbol{X}}), \tag{10}$$

$$\Xi = \sum_{i=1}^{t-1} \left\| \boldsymbol{X}_{i+1}^{k+1} - \boldsymbol{X}_i^k \right\|^2 = \left\{ \boldsymbol{M}(\boldsymbol{X}^k + d\boldsymbol{X}) \right\}^T \boldsymbol{M}(\boldsymbol{X}^k + d\boldsymbol{X}), \tag{11}$$

respectively, where $\boldsymbol{M}$ ($nt \times nt$ elements) is a square matrix. Only the diagonal and one sub-diagonal element of this matrix have non-zero values, 1 or -1, in order to add constrains for the same parameters in adjacent time-steps.

In our approach, the space-domain Lagrangian is expressed as a diagonal matrix $\hat{\Lambda}$ ($nt \times nt$ elements) because the active constraint balancing (ACB) is adopted for the space-domain regularization (Yi *et al.*, 2003). The time-domain Lagrangian is expressed as a diagonal matrix **A** (Karaoulis *et al.*, 2011) which offers flexibility to describe relatively rapid time changing phenomena. In particular, by allowing the time-Lagrangian multiplier to change in both space and time domain, the matrix $\boldsymbol{A}$ is a diagonal matrix with dimensions ($nt \times nt$ elements), where *n* is the number of the parameters of a space model at each reference time. Therefore, $\boldsymbol{A}$ can take discrete values for every space parameter of every time-step making the time-related regularization active. Obviously, if **A** is a zero matrix, then the 4D-ATC equation is transformed into independent inversions. From Eqs. (9) to (11), the final objective function *T* to be minimized is therefore given by:

$$T = \left\| \boldsymbol{e}^T \boldsymbol{e} \right\|^2 + (\partial^2 d\hat{\boldsymbol{X}})^T \hat{\Lambda} (\partial^2 d\hat{\boldsymbol{X}}) + \left\{ \boldsymbol{M}(\hat{\boldsymbol{X}}^k + d\hat{\boldsymbol{X}}) \right\}^T \boldsymbol{AM}(\hat{\boldsymbol{X}}^k + d\hat{\boldsymbol{X}}), \tag{12}$$

where the matrix $\hat{\Lambda}$ ($nt \times nt$ elements) denotes a diagonal matrix for the active constraint balancing (ACB) in the space domain (Yi *et al.*, 2003), $\hat{\Lambda} = \mathrm{diag}\left[\Lambda_1, \Lambda_2, \cdots, \Lambda_t \right]$, where $\boldsymbol{\Lambda}_i$ is the ACB matrix for the model at time *i*..

Minimizing the objective function given in Eq. (12) with respect to the model perturbation vector yields the following normal equations (Kim *et al.*, 2009):

$$\tilde{\boldsymbol{X}}^{k+1} = \tilde{\boldsymbol{X}}^k + d\tilde{\boldsymbol{X}}, \tag{13}$$

$$d\tilde{\boldsymbol{X}} = \left(\hat{\boldsymbol{j}}^T \hat{\boldsymbol{j}} + \hat{\boldsymbol{C}}^T \hat{\Lambda} \hat{\boldsymbol{C}} + \boldsymbol{M}^T \boldsymbol{AM} \right)^{-1} \left[\hat{\boldsymbol{j}}^T \left(G(\tilde{\boldsymbol{X}}^k) - \hat{\boldsymbol{D}} \right) - \boldsymbol{M}^T \boldsymbol{AM} \tilde{\boldsymbol{X}}^k \right]. \tag{14}$$

In Eq. (14), $\hat{\boldsymbol{j}}$ ($n_m t \times nt$ elements) denotes the sensitivity matrix (or Jacobian) and n_m the number of measurements from each time step. We consider that during the record of a single time-step data set $\boldsymbol{d}_i$, the changes of the conductivity of the subsurface can be neglected, $\hat{\boldsymbol{j}}$ can be expressed as a block diagonal matrix (Kim *et al.*, 2009):

$$\hat{\boldsymbol{j}} = \mathrm{diag}\left[\boldsymbol{J}_1, \boldsymbol{J}_2, \cdots, \boldsymbol{J}_t\right] = \begin{bmatrix} \boldsymbol{J}_1 & 0 & 0 & 0 \\ 0 & \boldsymbol{J}_2 & 0 & 0 \\ 0 & 0 & \ddots & 0 \\ 0 & 0 & 0 & \boldsymbol{J}_t \end{bmatrix}, \tag{15}$$

for a number t of distinct times. The matrix $\boldsymbol{J}_i$ denotes the sensitivity matrix at time i. For the definition and computation of the complex-valued sensitivity for the complex conductivity problem using the adjoint technique, we refer the readers to Kemna (2000). When the subsurface conductivity changes during each data acquisition, the assembled sensitivity matrix is no longer a block diagonal matrix as explained in Kim *et al.* (2009). The matrix $\hat{\boldsymbol{C}}$ is the differential operator in the space domain. It is given by $\hat{\boldsymbol{C}} = \mathrm{diag}\left[\boldsymbol{C}_1, \boldsymbol{C}_2, \cdots, \boldsymbol{C}_t\right]$, where $\boldsymbol{C}_i$ is the differential operator for the space-model of time i (Oldenburg *et al.*, 1993).

The active time Lagrangian, expressed with the matrix $\boldsymbol{A}$, controls the time-related changes. Effectively, such a scheme should vary the time normalization between the parameters of different time steps proportionally to the spatial resistivity changes occurring among different monitoring locations. The determination of the time regularization parameter may depend on the spatio-temporal characteristics of the process, which is controlling the changes in the complex resistivity. Ideally, matrix entries associated with areas of significant property changes must be assigned low time regularization values and vice-versa. Two methods are proposed to assign the appropriate values to the time regularization parameter: one based on a fast pre-estimation of the first independent inversion iteration and one, more accurate, after a full inversion (Karaoulis *et al.*, 2011). In this work we used the accurate calculation of the time Lagrange matrix.

The creation of the matrix ***A*** is similar to the DC (real values) problem with one exception. In the induced polarization case, two models must be considered, one for time-lapse changes in the amplitude and one for the time-lapse changes of the phase. Note that the resistivity and the phase can change over time independently from each other (see Vaudelet *et al.*, 2011a, b, for laboratory examples). The values of the Lagrangian parameters should be low for areas that show time-lapse changes in amplitude and/or phase.

To perform this task, we follow the following steps: (1) We generate a time-related distribution of values for the Lagrangian parameter as a function of the difference in amplitude between two sequential time-steps, (2) we generate a time-related distribution of values for the Lagrangian parameter from the difference in phase between two sequential time-steps and, (3) we combined these two time-related Lagrangian value distributions in one scheme (e.g., for a specific sub-region use as final value, the minimum value between amplitude and phase distributions). Trial-and-error testing showed that for our numerical examples the two time-related Lagrangian values must be between 0.01 and 0.1.

4. 3D Synthetic Test

The 4D-ATC algorithm is going to be tested with synthetic data and compared to the prediction of using independent inversion tomographies (performed independently at each time step). In the case of field data, it is expected that the artifacts associated with the presence of noise in the data is significant and independent inversion must be therefore avoided. In order for the comparison between the two approaches to be objective, all algorithms were based on the same 3D finite element forward modeling and inversion platform, the principles of this platform having already been discussed in Section 2 above.

Note that the same homogeneous half-space was used as the starting model for all the tested techniques, and that all the synthetic data are considered as measured simultaneously for each time step. In the present paper, the phase and amplitude are shown (it is implicit that the phases have negative values). The data misfit was smaller than 5% for the two examples discussed below.

4.1 Synthetic model and Time-Lagrangian distribution

Modeled data obtained for 5 different time steps representing a hypothetical time-lapse induced polarization change are depicted in Figures 1 and 2. A total of 225 surface electrodes were used to obtain surface dipole-dipole data (inter-electrode spacing a=1 with maximum intra-dipole spacing dn = 7). The pseudosection comprises a total of 945 measurements for each time-step. In this specific example, the synthetic data are taken noise-free. The background model had an amplitude of 10 Ohm m for the amplitude of the resistivity and 5 mrad for the amplitude of the phase.

Figures 1 and 2 show the modeled evolution of both the amplitude of the resistivity and the amplitude of the phase. The grey cubes show the changes (in both amplitude and phase), that remain stable through time. Red cubes reveal the modeled changes in both the amplitude of the resistivity and the amplitude of the phase between two sequential time steps. For instance, the red cube shown in time step 1 in amplitude, remains stable from time step 2 on (so it is denoted as grey in all later time steps), where a new red cube is introduced, which shows the modeled change between those two time steps.

As discussed in Section 4, the 4D-ATC technique requires *a priori* information on the expected time related changes, so the matrix $\boldsymbol{A}$ could be formulated. Figure 3 shows the distribution of the time Lagrangian values used as *a priori* information. The $\boldsymbol{A}$ matrix must consider time related changes in both amplitude and phase, in order to adjust appropriate weight. Cold colors, i.e. low values on the time-related Lagrangian, indicate areas with expected changes in both amplitude and phase, and hot colors (large time-related Lagrangian values) areas with no time changes. Therefore, Figure 3 shows, with gray cubes, the actual changes in both amplitude and phase in the same figure. The relation between low time-related Lagrangian values with the actual changes is quite good, even considering the fact that the estimation seems to be spread. Note that the ***A*** matrix is just a pre-estimation of where the expected change is located between two time steps. The ***A*** matrix was calculated using the full independent inversion of each data set. In Figures 4 and 5, the first series of images (upper part) shows the difference in amplitude between two sequential time steps; in Figures 6 and 7, the first series of images (upper part) denotes the difference in the phase. A combination of the amplitude and phase time-related changes is then used to create the matrix ***A*** (Figure 3).

4.2 Inversion results

The second rows of Figures 4 to 7 show the difference inversion images produced using the 4D-ATC technique. Grey cubes represent the modeled time changes. Generally, when compared with the independent inversion, inversion artifacts are reduced, and at the same time, the actual change is shown in a clearer way. The areas of the actual changes, when using the 4D-ATC technique, are represented in a more compact form, and as discussed in Section 4, the partial unsuccessful choice of pre-estimation when creating the matrix ***A***, does not affect the final difference images. Custom ***A*** matrices, based on more geological information than resistivity data, can significantly reduce artifacts and help focus on the real changes. Both techniques create an artifact of reduced phases between time-steps 3 and 4, which indicate the difficulties obtaining information when time-related changes are robust. In those cases, higher orders of time-specific regularization should be used.

Figure 8 shows the percentage RMS (root mean square) fit between the original (true) model and the final inversion result for every time step. 4D-ATC exhibits the smaller percentage model RMS misfit (real number), in all cases, except at time-step #1. The percentage error misfit regarding the magnitude of the phase is significantly larger than for the amplitude of the resistivity. This is due to the small expected values of the phase when compared to the amplitude (e.g., Kemna, 2000). This problem can be partially addressed using inversion techniques like final phase improvement (see Kemna, 2000) for which additional iterations are used only for the phase. Figures 9 and 10 show the final inversion models using the 4D-ATC technique. The grey cubes denote the modeled change. We observe that the inversion models are in good agreement with the true models.

5. ATC-based Tomography of a Salt Tracer Test

To investigate the effect of heterogeneity in the Earth's subsurface on the time-lapse ATC technique, a 2D stochastic model was used to simulate a salt tracer test injection. This stochastic model was used to generate a realistic synthetic dataset of the Earth subsurface to test the inversion algorithm.

5.1. Stochastically Generated Heterogeneous Aquifer

An heterogeneous aquifer with a stochastic distribution of the transport parameters was generated using the Stanford Geostatistical Modeling Software package (SGeMS, see Remy *et al.*, 2009). Several stochastic models were realized with the sequential Gaussian simulation algorithm (SGSIM, see Remy *et al.*, 2009, p. 135) on a 2D, 500 x 100 Cartesian grid, $\mathbf{h}(x, z)$, using an asymmetric semi-variogram for simple kriging defined as,

$$\gamma(\boldsymbol{h}) = c_0\gamma^0 + c_1\gamma^1(\boldsymbol{h}), \tag{16}$$

where $c_0\gamma^0$ is a nugget effect with constant c_0 = 10^{-3} and an anisotropic spherical Gaussian semi-variogram $c_1\gamma^1(\boldsymbol{h})$ with major, medium, and minor ranges of 75, 50, and 25, respectively, and a null (longitudinal) azimuth, dip, and rake. A single realization $\boldsymbol{m}$ was chosen to define the heterogeneous parametric distribution for the finite element simulations of the salt tracer test described below.

This geostatistical model was normalized and scaled as both linear and logarithmic distributions, such that $\boldsymbol{m}$ belongs to the interval (0, 1) for linearly distributed parameters and the logarithm (in base 10) of m belongs to the interval (0, N) for log-distributed parameters where N is the number of decades spanned by a given parameter. These models are shown in Figure 11. Parameters were mapped into the geostatistical model space by scaling $\boldsymbol{m}$ by a range of parameter values. For linearly distributed parameters (like the porosity ϕ), we use the following function,

$$\boldsymbol{m}_i = \boldsymbol{m}^i_{\min} + n\boldsymbol{m}\,, \tag{17}$$

where $\boldsymbol{m}_i$ is the mapped parameter distribution, $\boldsymbol{m}^i_{\min}$ is the lower limit of a given parameter i, and n is scalar defined as $n = \boldsymbol{m}^i_{\max} - \boldsymbol{m}^i_{\min}$. For log-distributed parameters, we use,

$$\boldsymbol{m}_i = \boldsymbol{m}^i_{\min} m\,. \tag{18}$$

For example, the permeability $\boldsymbol{k}$ is estimated to comprise values ranging from 10^{-12} m^2 to 10^{-17} m^2; hence, permeability is mapped to the model space with Eq. (18) using $\boldsymbol{m}^i_{\min}$ = 10^{-17} m^2 and $N = 5$.

The constitutive equations are Darcy's law for the Darcy velocity $\mathbf{u}$ (in m s^{-1}), a generalized constitutive equation for the flux density of the salt $\mathbf{j}_d$ (in kg m^{-2} s^{-1}) and including an advective tern in addition to the diffusion/dispersion term (Fick's law), and Ohm's law for the current density **j** (in A m^{-2}),

$$\mathbf{u} = \phi \mathbf{v} = -\frac{1}{\eta_f} k \nabla p \, , \tag{19}$$

$$\mathbf{j}_d = -\rho_f \phi \mathbf{D} \cdot \nabla C_m + \rho_f \phi \mathbf{v} C_m \, , \tag{20}$$

where **v** is the mean velocity of the pore water (m s^{-1}), **D** (in m^{2}s^{-1}) is the hydrodynamic dispersion tensor, p is the pore fluid pressure (in Pa), C_m is the solute mass fraction (dimensionless), and η_f is the dynamic viscosity of the fluid (in Pa s), and ρ_f is the mass density of the pore water (in kg m^{-3}). In addition to the constitutive equations, we have to consider two continuity equations for the mass of the pore water and for the mass of the salt,

$$\nabla \cdot (\rho_f \mathbf{u}) = -\frac{\partial(\rho_f \phi)}{\partial t} + \rho_f Q_s \, , \tag{21}$$

$$\nabla \cdot \mathbf{j}_d = -\frac{\partial(\rho_f \phi C_m)}{\partial t} + \rho_f Q_s C_m^0 \, , \tag{22}$$

where C_m^0 is the solute mass fraction of the salt in the source term, and Q_S is a volumetric hydraulic source term for the injection/abstraction of water (in s^{-1}). The effect of the salt concentration on the mass density and viscosity are neglected. In the so-called Fickian model, the hydrodynamic dispersion tensor is described by

$$\mathbf{D} = \left[\frac{D_m}{F\phi} + \alpha_T v \right] \mathbf{I}_3 + \frac{\alpha_L - \alpha_T}{v} \mathbf{v} \otimes \mathbf{v} \, , \tag{23}$$

where D_m is the molecular (mutual) diffusion coefficient of the salt (in m^2 s^{-1}) (for a NaCl solution, D_m is 1.60x10^{-9} m^2 s^{-1} at infinite dilution and 1.44x10^{-9} m^2 s^{-1} at high salinities at 25°C), $\mathbf{I}_3$ is the unit 3x3 tensor, $v = |\mathbf{v}|$, $\mathbf{a} \otimes \mathbf{b}$ represents the tensorial product between two vectors **a** and **b**, α_L and α_T are the longitudinal (along **v**) and transverse (normal to **v**) dispersivities (in m), and the product between the formation factor and the connected porosity represents the tortuosity of the pore space, which controls the macroscopic diffusion coefficient $D = D_m / F\phi$ (Revil, 1999) where F is the formation factor.

The finite element model is composed primarily of a single rectangular domain (100 m long by 20 m deep) defined as a function of the porosity ϕ, permeability k, and molecular diffusion coefficient D (see Table 1). The longitudinal and transversal dispersivities will be considered constants.

The in-phase and out-of-phase (quadrature) surface conductivities are determined from the model developed by Revil & Florsch (2010) and Revil & Skold (submitted to GJI, 2011). The mean grain diameter d_0 is computed from the permeability and the porosity $d_0 = (24\ F^3\ k)^{0.5}$ and $F = \phi^{-1.5}$ (Revil & Florsch, 2010). The salinity dependence of Σ_S is taken into account using the model developed by Revil & Florsch (2010, their Figure 12). Longitudinal α_L and transverse α_T dispersivities are related as $\alpha_T = 0.2\text{-}0.01\ \alpha_L$ where α_L is commonly assumed between 0.01 m and 0.1 m (see Bear, 1972). For our simulation, we use $\alpha_L = 1$ cm and $\alpha_T = 0.1$ cm. The effect of the salinity upon the electrical conductivity of the brine σ_f is accounted for by using the Sen & Goode (1992) model, which is valid from dilute concentrations to saturation in salt. When the induced polarization response is given by the model described in Revil & Florsch (2010) and when the surface conductivity term is small with respect to the pore water conductivity in the in-phase conductivity, the in-phase and quadrature conductivities are independent on the conductivity of the diffuse layer and the in-phase conductivity is nearly frequency independent.

A pressure differential is established across the domain by setting Dirichlet conditions at the inlet and outlet boundaries. The steady-state flow condition is on the order of $u = 0.1$ m s^{-1} across the domain. The geometry is shown in Figure 11. The injection of a high salinity brine $\rho_f\ C_m^0 = 500$ kg m^{-3} (salt saturation of the solution, 1000 times the background salinity of 0.5 kg m^{-3}) is simulated for a duration of 7 minutes in an upstream well at a bottom hole depth of 5 m (Figure 12). The total resultant flux of the salt within the model is simulated for 60 minutes. The resultant synthetic data comprises the transient amplitude and phase of the complex conductivity response computed at 1 Hz (see Figure 12). These data are inverted using the time-lapse ATC technique as described above in Section 3.

5.2.Modeling and Inversion Results

The inversion results are shown in Figure 13 and 14. We consider 48 electrodes with 2 meters spacing forming a total of 1422 dipole-dipole measurements per time-lapse data set. We assume that the time needed to take the data is short with respect to the characteristic time associated with the transport of the salt (true snapshots). In the field, the duration of an acquisition is not necessarily small with respect to the resistivity changes and this limitation will need to be investigated in a future work. The data RMS error for the time-lapse data set (difference between observed and calculated data) after 5 iterations was approximately 6%. Model RMS error varied from 6% up to 70%, depending on the complexity of the true model. It is important to note that the model RMS error in a stochastically generated model is expected to have high values, similarly to real data, since no inversion scheme can find both the actual values of amplitude and phase in each cell. This being said, the tomograms compare fairly well with the true resistivity and phase distribution both in correctly localizing the anomalies and reproducing the amplitudes. Note that the shape of the resistivity and phase anomalies are, however, not completely reproduced, mainly because the stochastic model uses quite anisotropic distributions of the permeability and porosity (i.e., a much larger correlation length in the horizontal direction than in the vertical direction). In turn, this implies that the change in brine concentration is also quite anisotropic. It is likely that better results could be achieved if a borehole would be used to assess the correlation length for the vertical resistivity distribution and this information would be used in the cost function.

6. Conclusions

The independent inversion of time-lapse induced polarization data may produce significant errors because of both errors in the measurements and errors in the inversion. These errors can lead to misleading interpretations of the monitored process. The 4D-ATC approach presented above reduces these errors while allowing relatively abrupt resistivity time-related changes in the areas where there are significant indications of these changes. It removes a good fraction of the artifacts associated with noise in the data that is uncorrelated over time. The 4D-ATC algorithm requires a pre-estimation of the position of the changing area. A method to estimate where those changes occur is to use the difference in the tomograms obtained from the independent inversions of the measurements at each time-step. It may be useful to use higher-order time-related regularizations in the 4D-ATC scheme. Numerical tests show that our approach works well on both a simple 3D synthetic case study and on a 2D simulation of a salt tracer transport in an heterogeneous synthetic aquifer. It is important to note, that although inversion convergence was in all cases less than 5%, the model misfit is always larger. This observation is due the fact that inversion is an ill-posed problem, and we cannot expect to find the exact complex conductivity values in each cell. In our work, the following assumptions were made: (i) the material properties vary linearly in time between two subsequent reference models, (ii) the acquisition time of a single time-step is neglected (the time considered to take a snaphot is instantaneous, which for SIP data acquisition is generally untrue) and (iii) the effect of the salt concentration on the mass and viscosity were neglected in the second numerical test.

It could be interesting to perform a joint inversion of complex resistivity data with the self-potential data for salt tracer injection tests. Self-potential monitoring has been shown recently to be very useful to follow salt tracer tests (Martínez-Pagán *et al.*, 2010; Revil & Jardani, 2010). However, the inversion of self-potential data is an ill-posed and underdetermined geophysical problem too. Because the sensitivity maps of self-potential and induced polarization data are however quite different, these two types of geophysical data are naturally suited for a joint inversion problem to better follow salt tracer tests and then to use the results to invert the permeability and dispersivity tensor distributions in the subsurface.

Acknowledgments. We thank Office of Science (BER), US. Department of Energy (Grant No. DE-FG02-08ER646559), NSF (SmartGeo Educational Program, Project IGERT: Intelligent Geosystems; DGE-0801692), and the U.S.EPA (Student Service Contract #EP10D00437) for financial supports. Although this work was reviewed by U.S.EPA and approved for presentation, it may not necessarily reflect official Agency policy. Mention of trade names or commercial products does not constitute endorsement or recommendation by U.S.EPA for use. We gratefully acknowledge fruitful discussions with Roland Martin (Bonn University) regarding the extension and testing of the inversion algorithm to the complex case. We thank Joerg Renner and two referees for their useful comments.

References

Atekwana, E.A., Atekwana, E., Werkema, D.D., Allen, J.P., Smart, L.A., Duris, J.W., Cassidy, D.P., Sauck, W.A. & Rossbach, S., 2004. Evidence for microbial enhanced electrical conductivity in hydrocarbon-contaminated sediments, *Geophys. Res. Lett.*, **31**, L23501.

Bear, J., 1972. *Dynamics of Fluids in Porous Media*, Elsevier Scientific Publishing Co.

Binley A., Slater L., Fukes, M. & Cassiani G., 2005. The relationship between frequency dependent electrical conductivity and hydraulic properties of saturated and unsaturated sandstone, *Water Resour. Res.*, **41**, 13, W12417.

Börner, F., Gruhne, M. & Schön J., 1993. Contamination indications derived from electrical properties in the low frequency range, *Geophysical Prospecting*, **41**, 83-98.

Börner, F.D., Schopper, W. & Weller, A., 1996. Evaluation of transport and storage properties in the soils and groundwater zone from induced polarization measurements, *Geophys. Prospect.*, **44**, 583-601, doi:10.1111/j.1365-2478.1996.tb00167.x.

Daily, W., Ramirez, A., LaBrecque, D. & Nitao, J., 1992. Electrical resistivity tomography of vadose water movement, *Water Resour. Res.*, **28**, 1429-1442.

Daily, W. & Ramirez, A.L., 2000. Electrical imaging of engineered hydraulic barriers, *Geophysics,* **65**, 83-94.

de Lima, O.A.L., & Sharma, M.M., 1992. A generalized Maxwell–Wagner theory for membrane polarization in shaly sands, *Geophysics*, **57**, 431–440.

Dey, A. & Morrison, H.F., 1979. Resistivity modeling for arbitrarily shaped three-dimensional structures, *Geophysics*, **44**, 753–780.

Flores Orozco, A., Williams, K.H., Long, P.E., Hubbard, S.S., and Kemna, A., 2011. Using complex resistivity imaging to infer biogeochemical processes associated with bioremediation of a uranium-contaminated aquifer: J. Geophys. Res., in press.

Florsch, N., Llubes, M., Téreygeol, F., Ghorbani, A. & Roblet, P., 2010. Quantification of slag heap volumes and masses through the use of induced polarization: application to the Castel-Minier site, *Journal of Archaeological Science*, in press, 1-14.

Ghorbani, A., Camerlynck C., Florsch N., Cosenza P., Tabbagh, A. & Revil A., 2007. Bayesian inference of the Cole-Cole parameters from time and frequency-domain induced polarization, *Geophysical Prospecting*, **55**(4), 589-605, doi: 10.1111/j.1365-2478.2007.00627.x.

Hördt, A., Blaschek, R., Kemna, A. & Zisser, N., 2007. Hydraulic conductivity estimation from induced polarisation data at the field scale—the Krauthausen case history, *J. Appl. Geophys.,* **62**, 33–46.

Karaoulis, M.,. Kim, J.-H. & Tsourlos, P.I., 2011. 4D Active Time Constrained Inversion, *Journal of Applied Geophysics*, **73**, 25-34.

Kemna, A., & Binley, A., 1996. Complex electrical resistivity tomography for contaminant plume delineation, *Proc. 2nd Mtg. Environmental and Engineering Geophysics, Environ. Eng. Geophys. Soc., Eur. Section*, 196-199.

Kemna, A., 2000. *Tomographic inversion of complex resistivity-theory and application*, Ph.D Dissertation, Ruhr-University of Bochum, Germany, 196 pp.

Kemna, A., Binley, A., Ramirez, A. & Daily, W., 2000. Complex resistivity tomography for environmental applications, *Chem. Eng. J*., **77**, 11-18.

Kemna A., Binley, A. & Slater L., 2004. Crosshole IP imaging for engineering and environmental applications, *Geophysics*, **69**, 1, 97-101.

Kim J.-H., Yi, M.J., Park, S.G. & Kim, J.G., 2009. 4-D inversion of DC resistivity monitoring data acquired over a dynamically changing earth model, *Journal of Applied Geophysics*, **68**(4), 522-532.

Legaz, A., Vandemeulebrouck J., Revil A., Kemna A., Hurst A. W., Reeves, R. & Papasin, R., (2009), A case study of resistivity and self-potential signatures of hydrothermal instabilities, Inferno Crater Lake, Waimangu, New Zealand, *Geophys. Res. Lett*., **36**, L12306, doi:10.1029/2009GL037573.

Leroy, P., Revil, A., Kemna, A., Cosenza, P., & Gorbani A., 2008. Spectral induced polarization of water-saturated packs of glass beads, *Journal of Colloid and Interface Science*, **321**(1), 103-117.

Leroy, P. & Revil A., 2009. Spectral induced polarization of clays and clay-rocks, *Journal J. geophy. Res*., **114**, B10202, doi:10.1029/2008JB006114.

Lesmes, D.P. & Morgan F.D., 2001. Dielectric spectroscopy of sedimentary rocks, *J. geophy. Res.,* **106** (B7) 13329-13346.

Lima, O. A. L., & Sharma, M. M., 1992. A generalized Maxwell-Wagner theory for membrane polarization in shalty sands, *Geophysics*, **57,** 431-440.

Looms, M.C., Jensen, K.H., Binley, A. & Nielsen, L., 2008. Monitoring unsaturated flow and transport using cross-borehole geophysical methods, *Vadose Zone Journal,* **7**, 227-237.

LaBrecque, D. J. & Yang, X., 2001, Difference inversion of ERT data: a fast inversion method for 3-D in situ monitoring, *Journal of Environmental and Engineering Geophysics*, **5**, 83-90.

Lane, J.W., Day-Lewis, F.D. & Casey, C.C., 2006. Geophysical monitoring of a field-scale biostimulation pilot project, *Ground Water*, **44**(3), 430-443

Loke, M. H., Chambers, J.E. & Ogilvy R.D., 2006. Inversion of 2D spectral induced polarization imaging data, *Geophysical Prospecting*, **54**, 287–301

Loke, M. H., 1999, Time lapse resistivity imaging inversion, Proceedings of the 5th Meeting of the Environmental and Engineering European, Em1, Budapest, Hungary.

Martínez-Pagán P., Jardani A., Revil A., & Haas A., 2010. Self-potential monitoring of a salt plume, *Geophysics*, **75**(4), WA17–WA25, doi: 10.1190/1.3475533.

Müller, K., Vanderborght, J., Englert, A., Kemna, A., Huisman, J.A., Rings, J. & Vereecken, H., 2010, Imaging and characterization of solute transport during two tracer tests in a shallow aquifer using electrical resistivity tomography and multilevel groundwater samplers, *Water Resour. Res.*, **46**, W03502. doi:10.1029/2008WR007595.

Nimmer, R.E., Osiensky, J.L., Binley, A.M., Sprenke, K.F. & Williams, B.C., 2007. Electrical resistivity imaging of conductive plume dilution in fractured rock, *Hydrogeology Journal*, **5**, 877-890.

Nguyen, F., Kemna, A., Antonsson, A., Engesgaard, P., Kuras, O., Ogilvy, R., Gisbert J., Jorreto, S. & Pulido-Bossch, A., 2009. Characterization of seawater intrusion using 2D electrical imaging, *Near-Surface Geophysics*, **7**(5-6), 377-390.

Nordsiek, S. & Weller, A., 2008. A new approach to fitting induced polarization spectra, *Geophysics*, **73**, F235eF245, doi:10.1190/1.2987412.

Ogilvy, R D., Kuras, O., Meldrum, P I., Wilkinson, P B., Chambers, J. E., Sen, M., Gisbert, J., Jorreto, S., Frances, I.,Pulido Bosch, A. & Tsourlos, P., 2009. Automated time-Lapse Electrical Resistivity Tomography (ALERT) for monitoring Coastal Aquifers. *Near Surface Geophysics*, **7**(5-6), 367-375.

Olhoeft, G. R., 1985. Low-frequency electrical properties, *Geophysics,* **50**, 2492-2503.

Olhoeft, G. R., 1986. Direct detection of hydrocarbon and organic chemicals with ground-penetrating radar and complex resistivity: Petroleum, hydrocarbons and organic chemicals in ground water-Prevention, Detection, and Restoration, *NWWA/API, Proceedings*, 284–305.

Park, S, 1998. Fluid migration in the vadose zone from 3-D inversion of resistivity monitoring data, *Geophysics*, **63**(1), 41-51

Pelton, W.H., Ward, S.H., Hallof, P.G., Sill, W.R. & Nelson, P.H., 1978. Mineral discrimination and removal of inductive coupling with multifrequency IP, *Geophysics,* **43**, 588–609.

Ramirez, A., Daily, W., LaBrecque, D., Owen, E. & Chesnut, D., 1993. Monitoring an underground steam injection process using electrical resistance tomography, *Water Resour. Res*., **29**, 73-87.

Revil A., 1999. Ionic diffusivity, electrical conductivity, membrane and thermoelectric potentials in colloids and granular porous media: a unified model, *Journal of Colloid and Interface Science*, **212**, 503-522.

Revil, A., & Jardani A., 2010. Stochastic inversion of permeability and dispersivities from time lapse self-potential measurements: A controlled sandbox study, *Geophys. Res. Lett*., **37**, L11404, doi:10.1029/2010GL043257.

Revil, A. & N. Florsch, N., 2010. Determination of permeability from spectral induced polarization data in granular media, *Geophys. J. Int*.,, **181**, 1480-1498, doi: 10.1111/j.1365-246X.2010.04573.x.

Revil, A., Cathles, L.M., Losh, S., & Nunn, J.A., 1998. Electrical conductivity in shaly sands with geophysical applications, *J. geophy. Res.,* **103**(B10), 23,925-23,936.

Routh, P.S., Oldenburg D.W., & Li, Y., 1998. Regularized inversion of spectral IP parameters from complex resistivity data. 68th SEG Meeting, New Orleans, USA, Expanded Abstracts, 810-813.

Seigel, H., Nabighian, M., Parasnis, D.S. & Vozoff, K., 2007. The early history of the induced polarization method, *The Leading Edge*, **3**, 312-321.

Sen, P.N., & Goode, P.A., 1992. Influence of temperature on electrical conductivity on shaly sands, *Geophysics*, **57**, 89-96.

Schmutz M., Revil, A., Vaudelet, P., Batzle, M., Femenía Viñao, P., & Werkema, D. D., Influence of oil saturation upon spectral induced polarization of oil bearing sands, *Geophys. J. Int*., **183**, 211–224, doi: 10.1111/j.1365-246X.2010.04751.x.

Shi, W., Rodi, W., & Morgan, F. D., 1998. 3-D induced polarization inversion using complex electrical resistivities: *Proc. Symp. Application of Geophysics to Engineering and Environmental Problems, Environ. Eng. Geophys. Soc*., 785-794.

Tsourlos P. 1995. *Modeling, interpretation and inversion of multielectrode resistivity data*. Ph-D Thesis, University of York, 315 pp.

Tsourlos, P., Ogilvy, R.D., Meldrum, P.I. & Williams, G.M., 2003. Time-lapse Monitoring in Single Boreholes Using Electrical Resistivity Tomography, *Journal of Environmental and Engineering Geophysics*, **8**(1), 1-14.

Vanhala, H., 1997. Mapping Oil-Contaminated Sand and Till with the Spectral Induced Polarization (SIP) method, *Geophysical Prospecting*, **45**, 303-326

Vaudelet, P., Revil, A., Schmutz, M., Franceschi, M. & Bégassat P., 2011a. Induced polarization signature of the presence of copper in saturated sands, *Water Resour. Res.,* **47**, W02526, doi:10.1029/2010WR009310.

Vaudelet, P., Revil, A., Schmutz, M., Franceschi, M. & Bégassat, P., 2011b. Changes in induced polarization associated with the sorption of sodium, lead, and zinc on silica sands, *Journal of Colloid and Interface Science*, **360**, 739-752.

Vinegar, H.J. & Waxman, M.H., 1984. Induced polarization of shaly sands, *Geophysics,* **49,** 1267–1287.

Waxman M.H. & Smits L.J.M., 1968. Electrical conductivities in oil-bearing sands, *Soc. Pet. Eng. J.*, **8**, 107-122.

Weller, A., Seichter, M. & Kampke, A., 1996. Induced-polarization modeling using complex electrical conductivities, *Geophys. J. Int.*, **127**, 387–398.

Williams, K.H., Kemna, A., Wilkins, M.J., Druhan, J., Arntzen, E., N'Guessan, A.L., Long, P.E., Hubbard, S.S., & Banfield, J.F., 2009. Geophysical monitoring of coupled microbial and geochemical processes during stimulated subsurface bioremediation, *Environ. Sci. Technol.*, **43**, 6717-6723, doi:10.1021/es900855j.

Yi, M.J., Kim, J.H. & Chung, S.H., 2003. Enhancing the resolving power of least-squares inversion with active constraint balancing, *Geophysics*, **68**, 931-941.

Zhang, Y., Ghodrati, A. & Brooks, D.H., 2005. An analytical comparison of three spatio-temporal regularization methods for dynamic linear inverse problems in a common statistical framework, *Inverse Problems*, **21**, 357–382.

Table 1. Stochastic parameters used in the geostatistical model used for the simulation of the salt tracer test.

Parameter	$m^i_{\min}$	$m^i_{\max}$	n, N
Porosity, ϕ (−)	0.25	0.35	0.1
Permeability, k (m^2)	10^{-17}	10^{-12}	5.0
Diffusion coefficient D (m^2 s^{-1}) [1]	10^{-12}	10^{-9}	3.0

1. Defined as the ratio between the molecular diffusion coefficient of the salt in water by the tortuosity, which is obtained by the product of the formation factor with the connected porosity)

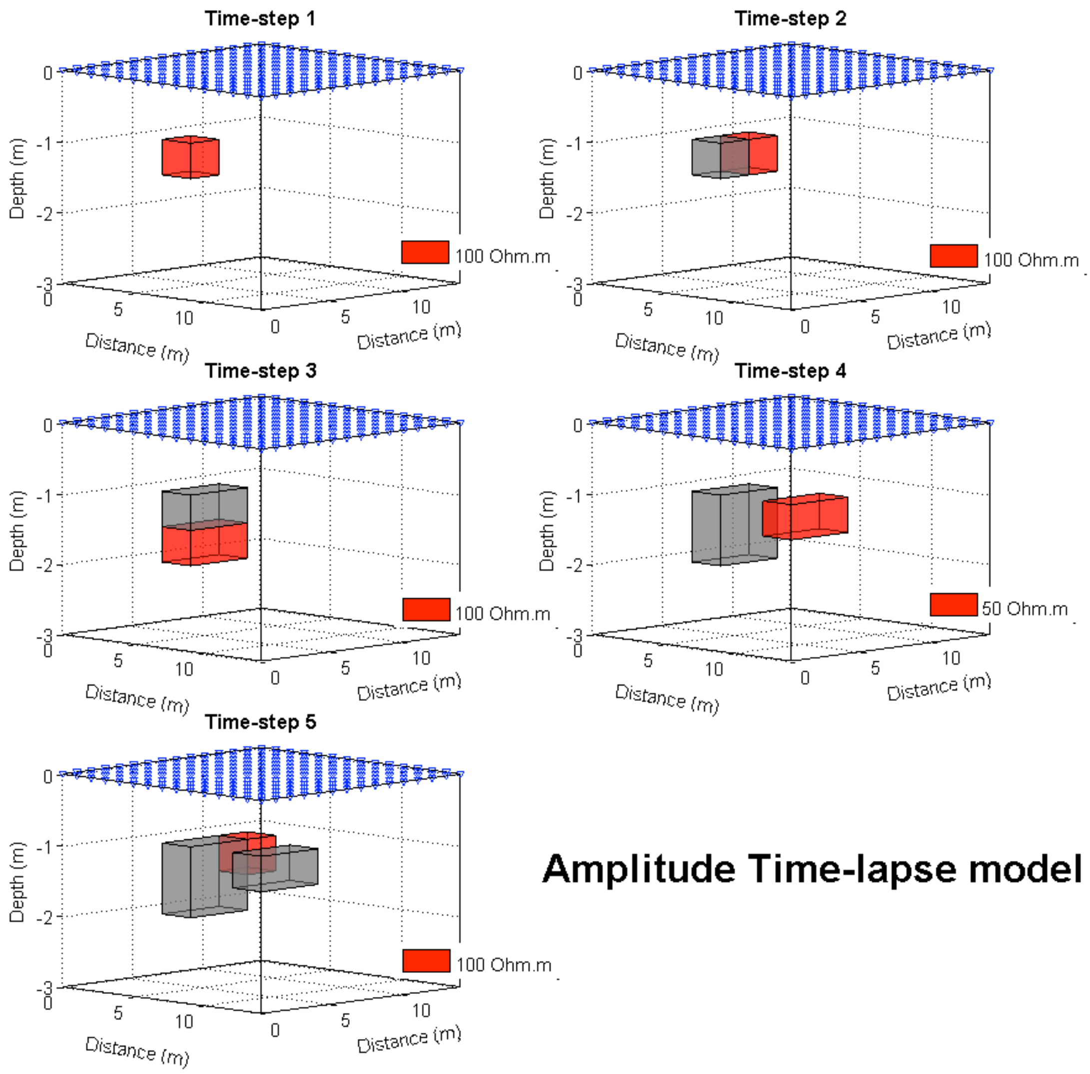

Figure 1. The 4D induced polarization model used in this work showing the changes in amplitude through time (five time-steps). The grey cubes denote the synthetic model used in the previous time-step. The red cubes show the change in that time-step with respect to the previous time-steps. The background model has a constant resistivity amplitude of 10 Ohm m.

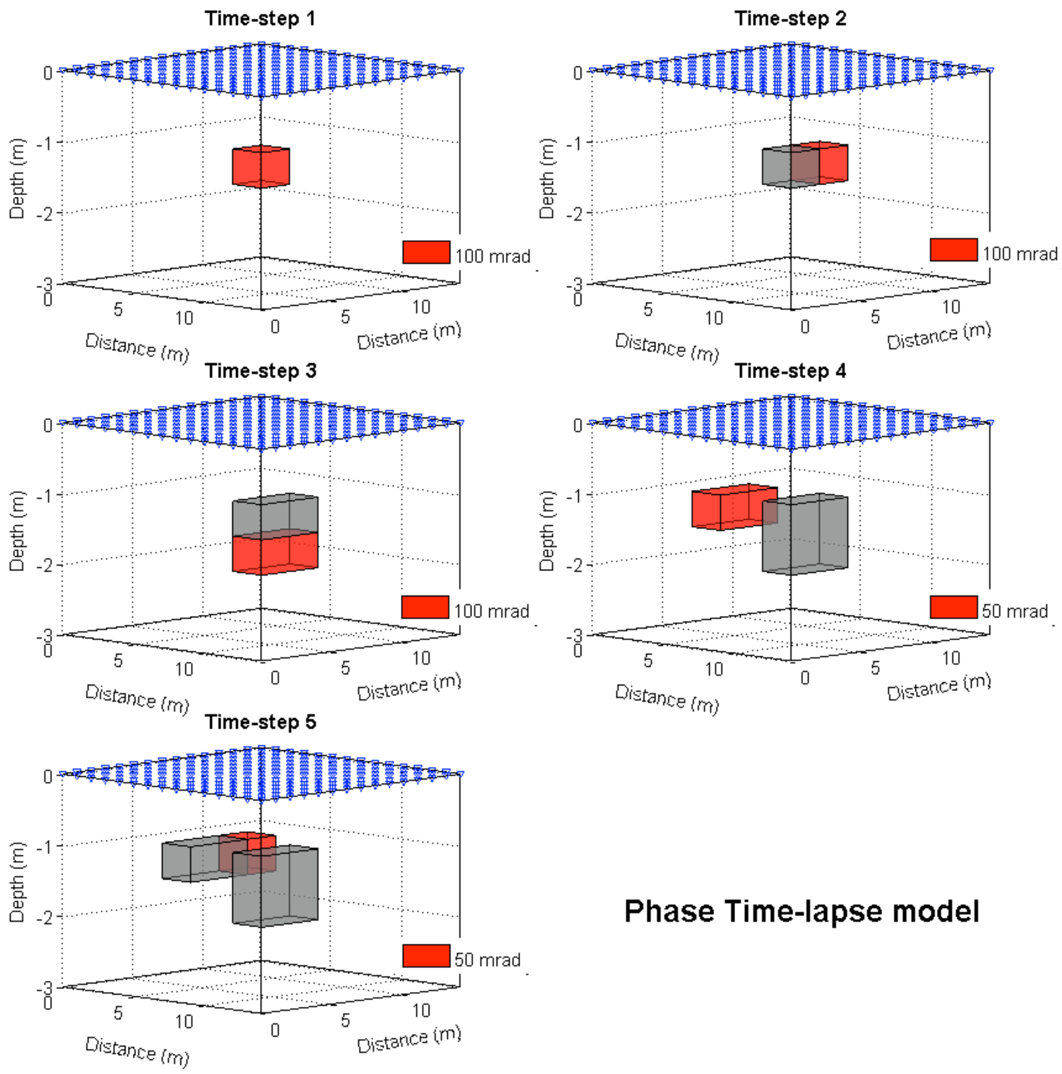

Figure 2. Same as Figure 1 for the phase lag. The background model has a phase of -5 mrad.

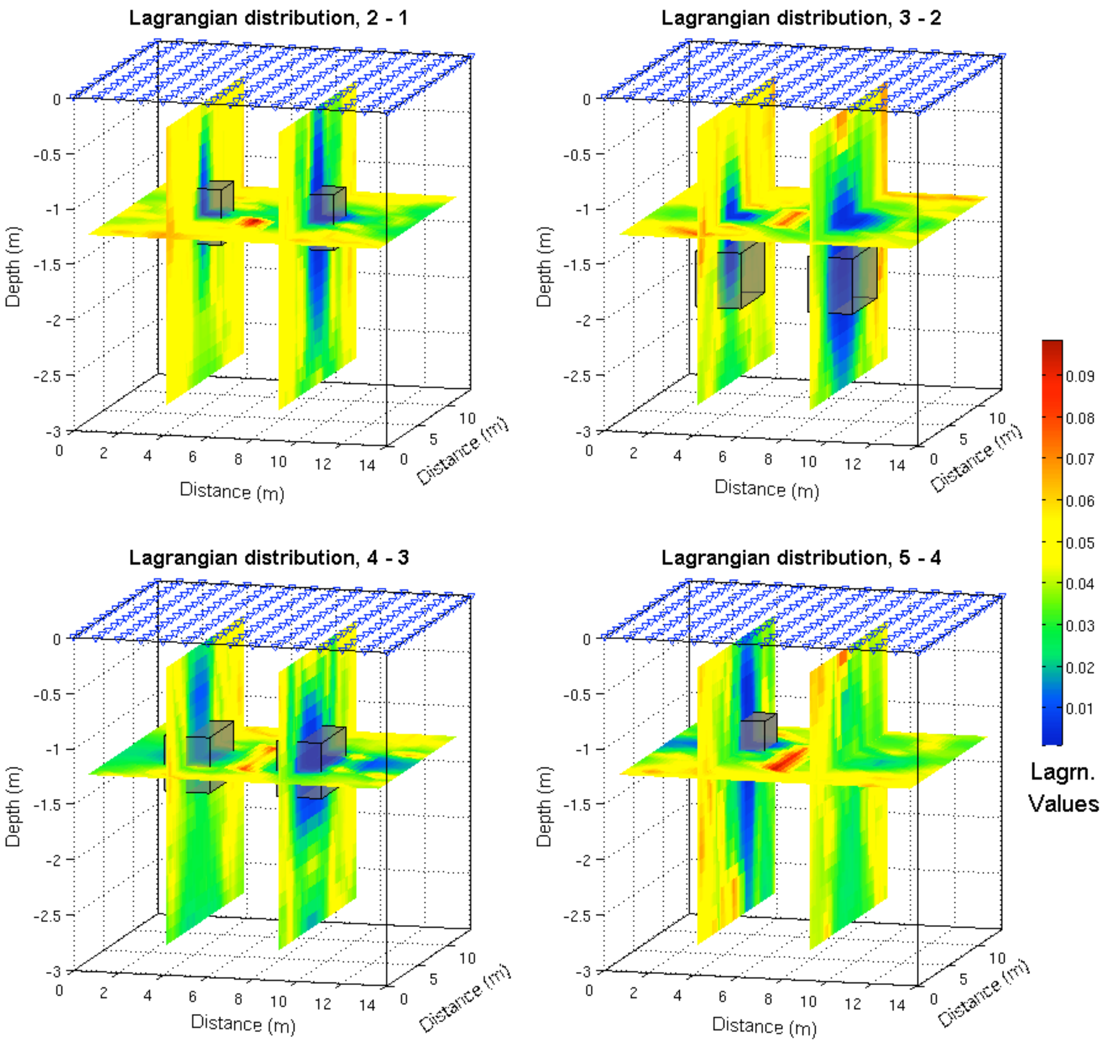

Figure 3. The distribution of lagrange parameters based on the independent inversion as a prior information used in the ATC approach. The cold colors indicate areas with significant changes. These areas are characterized by low values of the Lagrange parameters. The hot colors indicate areas with no changes, i.e., areas characterized by high values of the (Lagrange) regularization parameters. The grey cubes show the position of the true changes in the synthetic model.

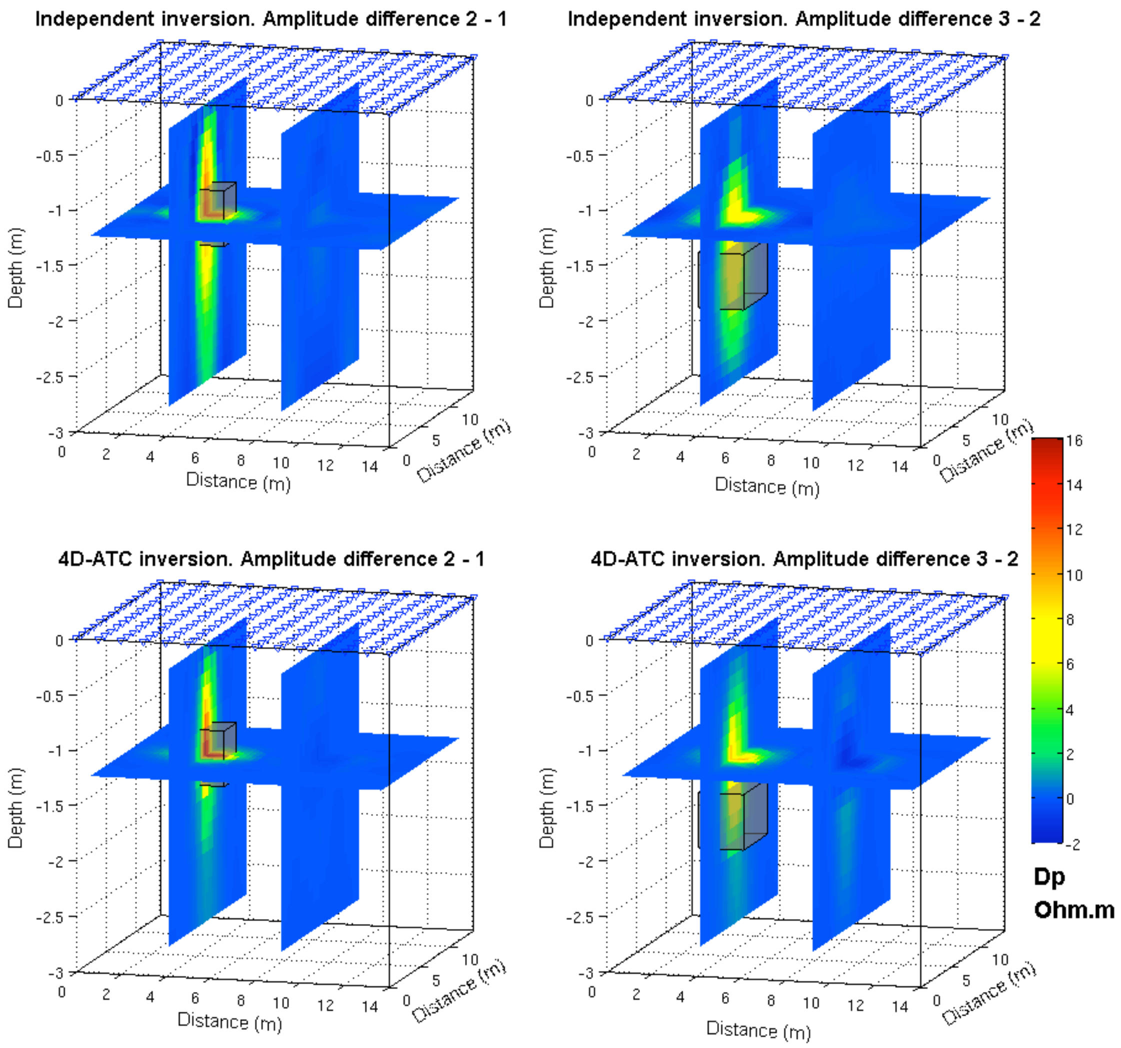

Figure 4. Difference images for the synthetic model of resistivity presented in Figures 1 and 2. The 4D-ATC (lower row) and independent inversion (upper row) difference amplitude images are shown for time steps 2-1 (left side) and 3-2 (right side), respectively. The grey cube shows the position of the true change according to the synthetic model.

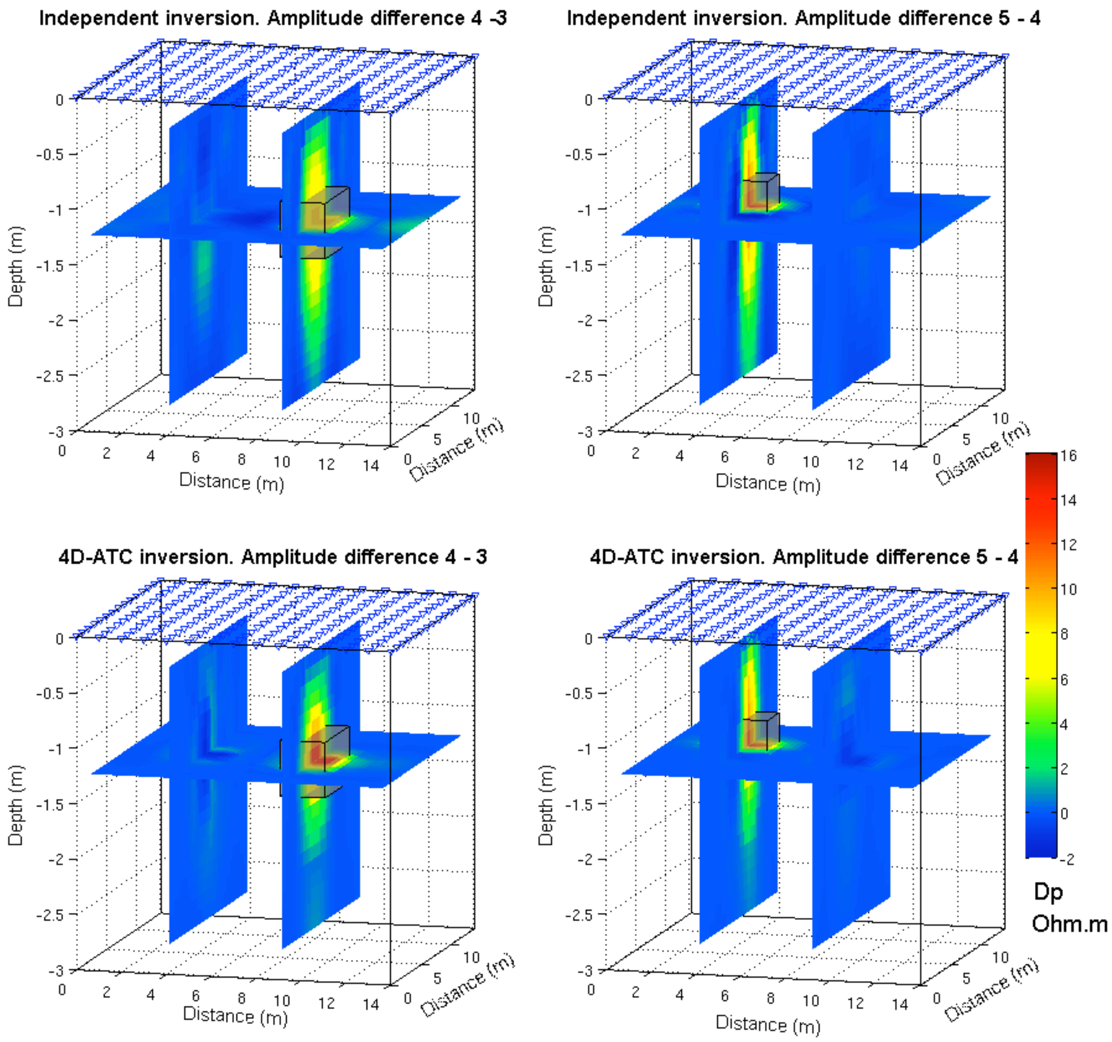

Figure 5. Difference images for the synthetic model presented in Figures 1 and 2. The 4D-ATC (lower row) and independent inversion (upper row) difference amplitude images are shown for time steps 4-3 (left side) and 5-4 (right side), respectively. The grey cube shows the localization of the true change from the synthetic model.

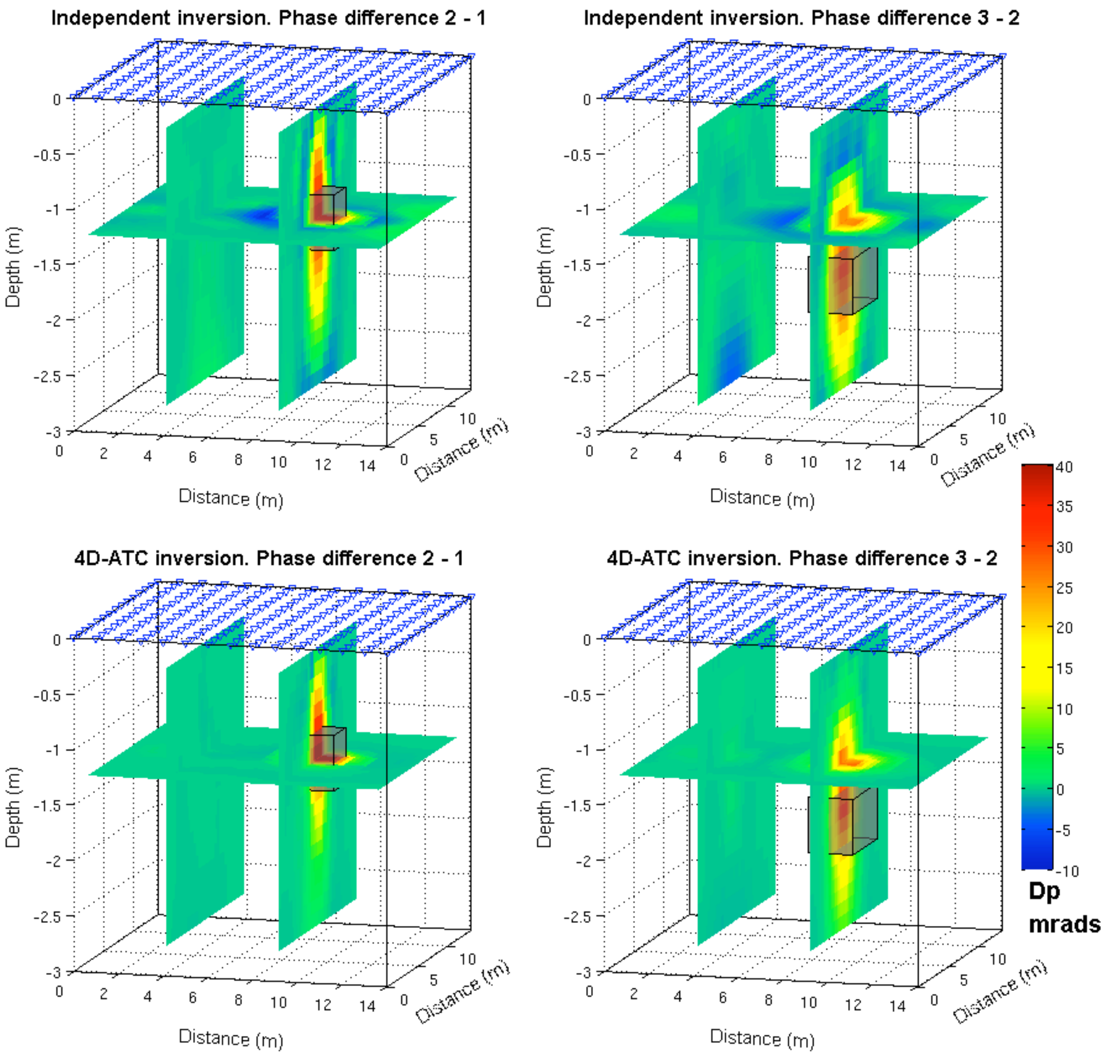

Figure 6. Same as Figure 4 for the phase.

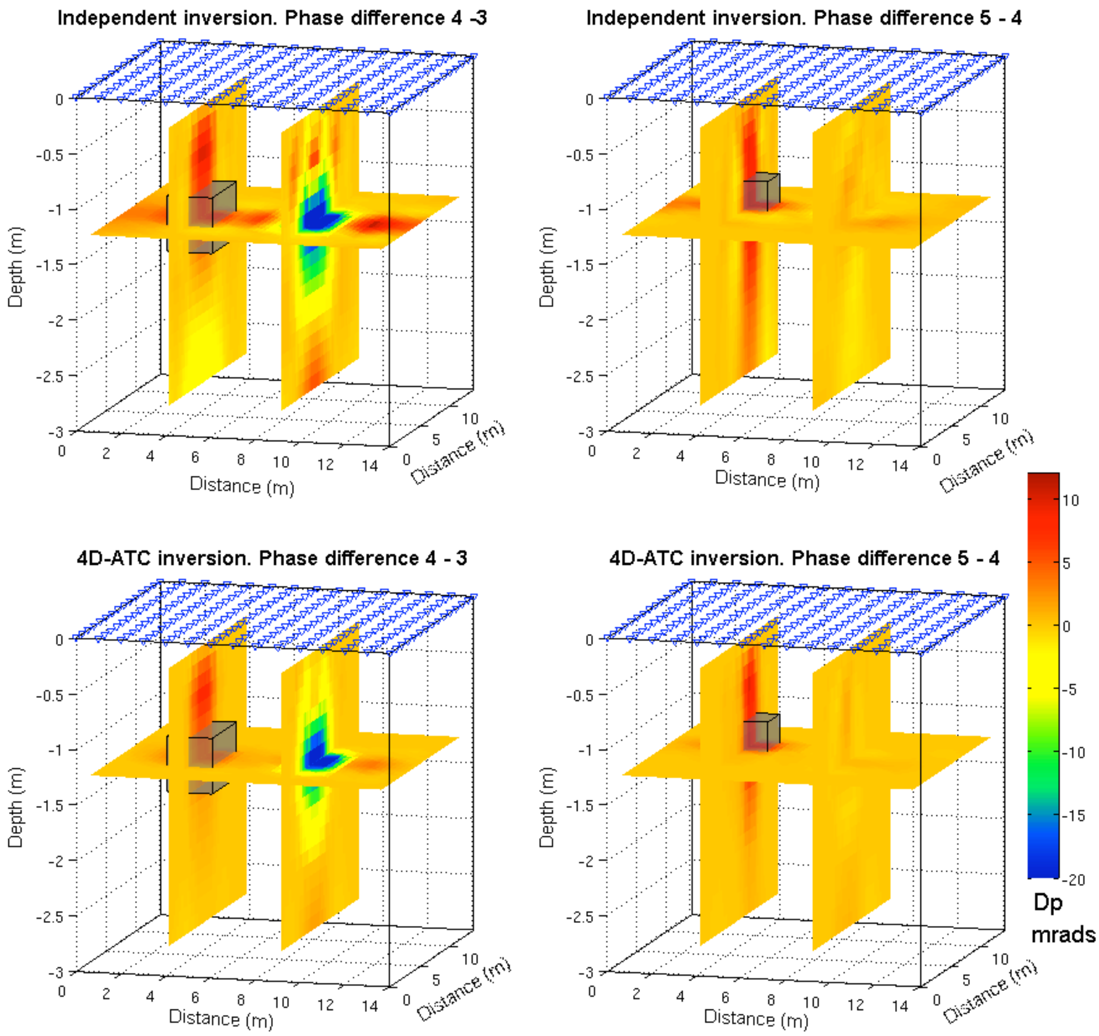

Figure 8. Same as Figure 5 for the phase.

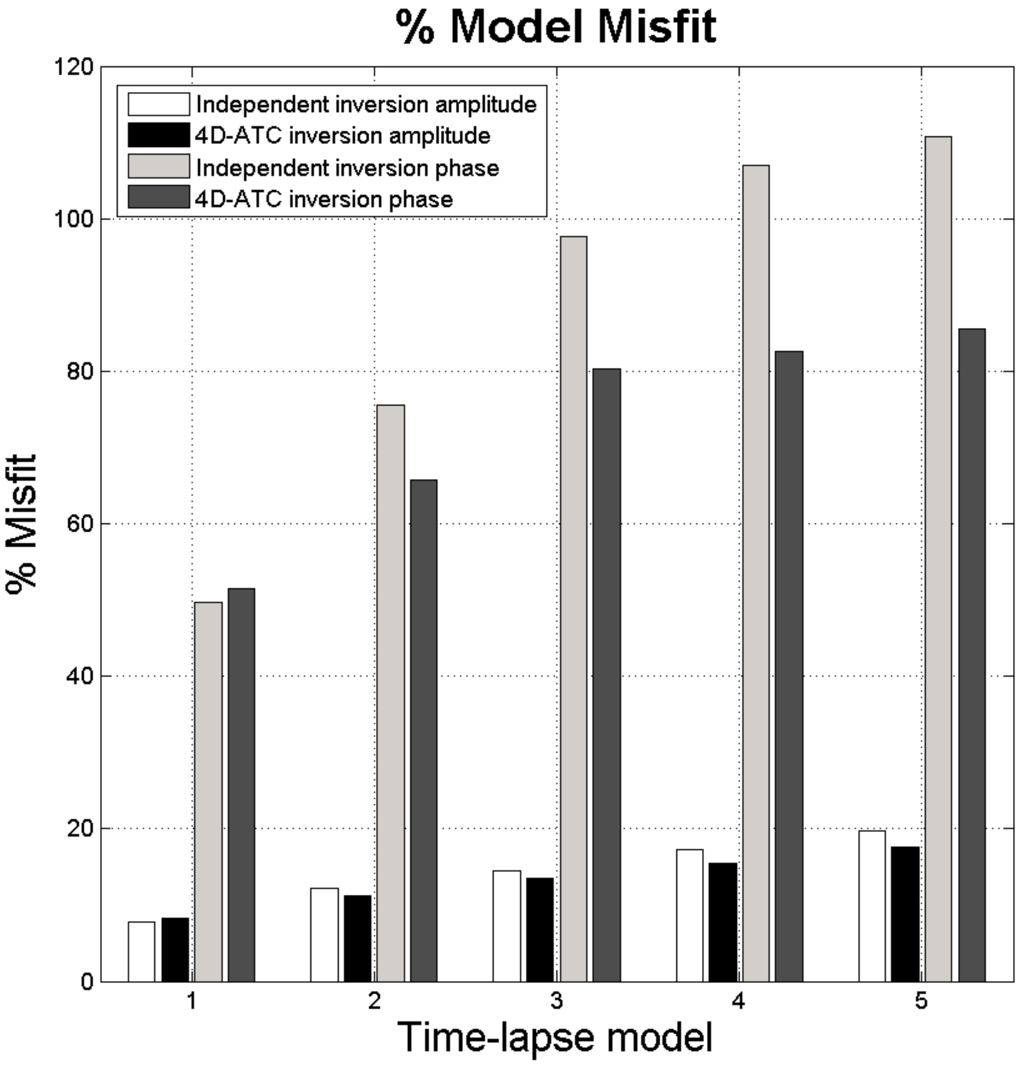

Figure 8. Percent model misfit for independent and 4D-ATC inversion (amplitude and phase). Note the lower RMS error associated in general with the ATC-based approach, in both the amplitude and phase. The lower % model misfit error between the inversion methods is an indication that the 4D-ATC approach produces a more realistic model.

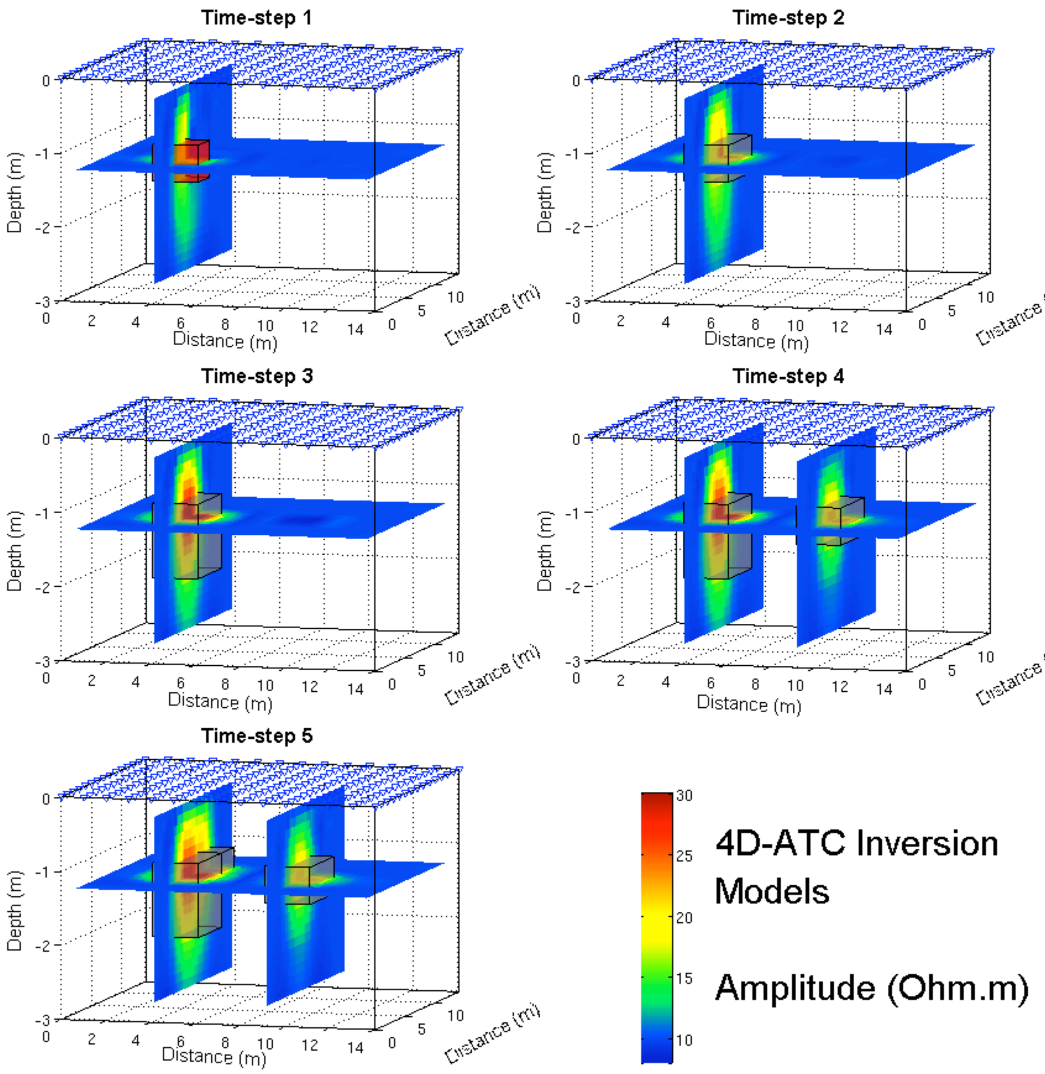

Figure 9. 4D-ATC inversion model showing the amplitude of each model time-step. The grey cube shows the true change in the amplitude of the resistivity.

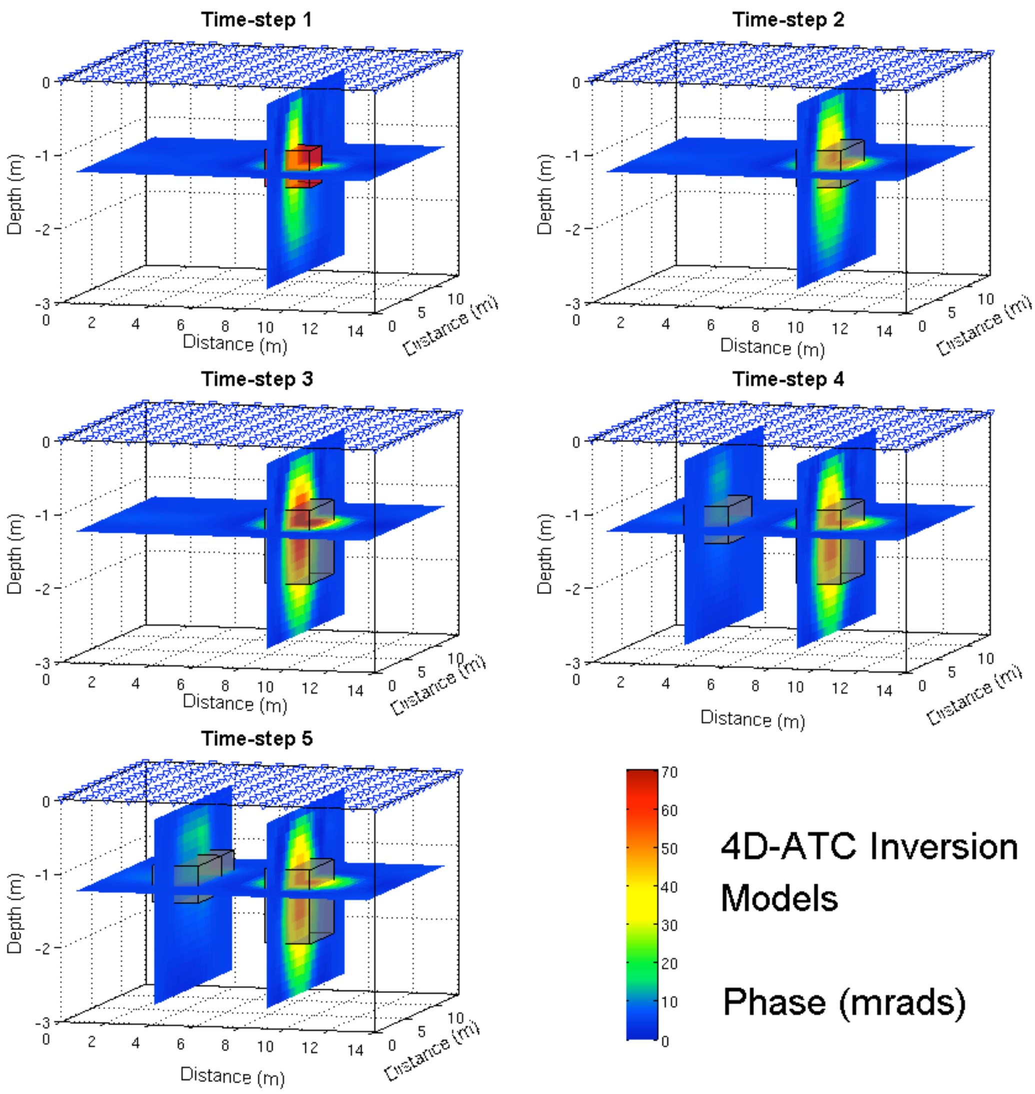

Figure 10. 4D-ATC inversion model of the phase at different time-steps. The grey cubes show the localization of the true changes in the phase.

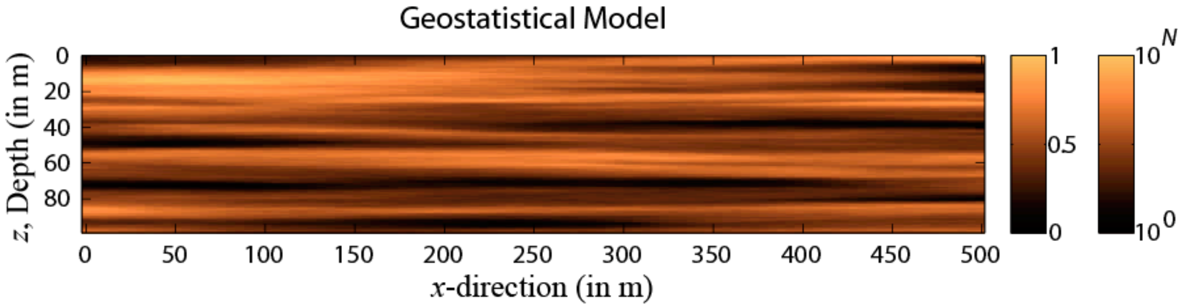

Figure 11. Geostatistical 2D model used for the simulation of the salt tracer test injection. This synthetic aquifer is generated with a horizontal correlation length that is stronger than the vertical correlation length. The water flows from the left to the right. Each cell is characterized by an isotropic frequency-dependent resistivity. The injection point for the salt injection is located at x = 5 m and z = 5 m. Only a subset of this domain is used for the time-lapse induced polarization test. The flow is from left to right.

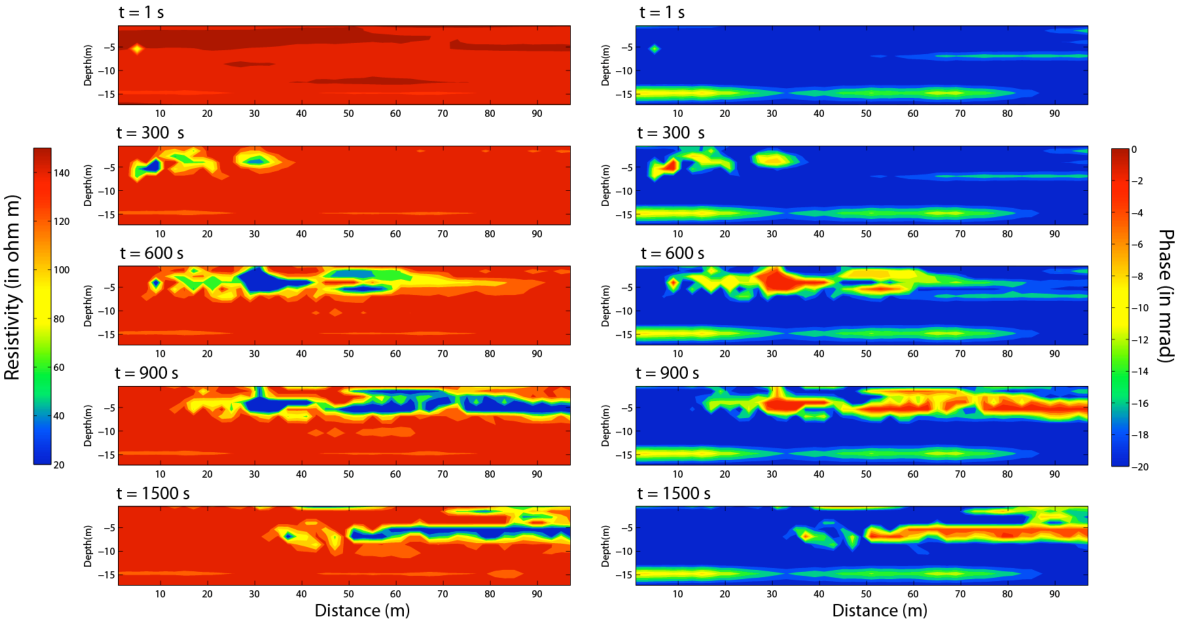

Figure 12. Result from the forward finite element modeling of the salt tracer test in terms of resistivity and phase at five different time steps (five snapshots). The phase accounts for both the effect of the resistivity and the influence of the salinity upon the quadrature conductivity through the dependence of the Stern layer surface conductivity on the salinity. The injection point for the salt is located at x = 5 m ad z = -5 m.

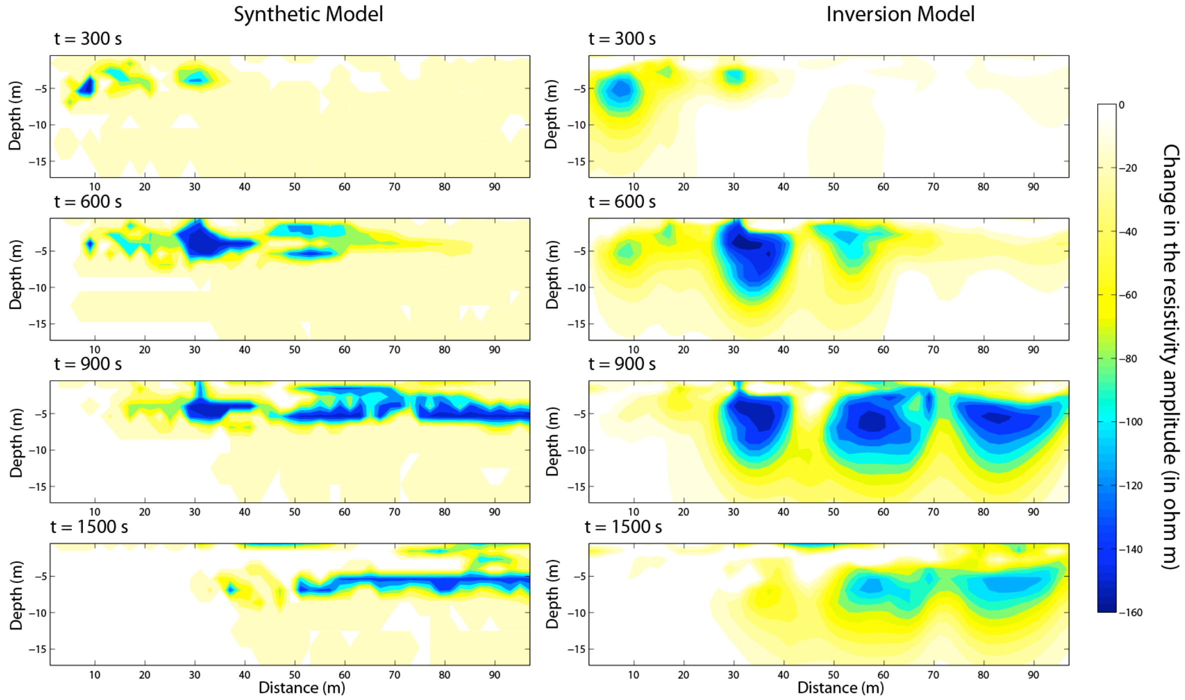

Figure 13. Comparison between the true resistivity changes from the forward model and the resistivity changes resulting from the time-lapse inversion of the apparent resistivity data collected from the top surface of the aquifer and contaminated with some noise. The results of the inversion are biased because we have assumed no prior knowledge of the anisotropy of the resistivity distribution of the medium.

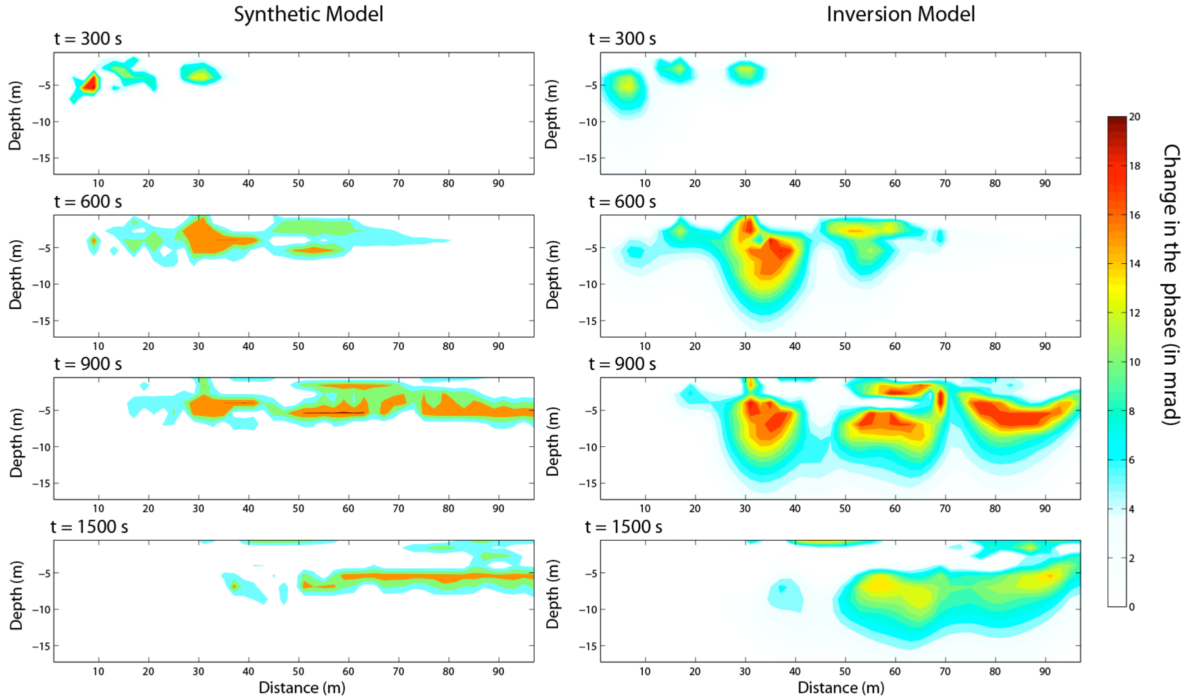

Figure 14. Comparison between the true changes of the phase (from the forward modeling associate with the simulation of the salt dispersion/advection problem) and the changes in the phase resulting from the time-lapse inversion of the apparent resistivity data and phase lags collected at the surface of the aquifer and contaminated with noise. The results of the inversion are biased because we have assumed no prior knowledge of the anisotropy of the resistivity distribution of the medium.